

# Role of Defects in Ultra-high Gain in Fast Planar Tin Gallium Oxide UV-C Photodetector by MBE

Partha Mukhopadhyay,<sup>1, a)</sup> Isa Hatipoglu,<sup>2</sup> Ymir K. Frodason,<sup>3</sup> Joel B. Varley,<sup>4</sup> Martin S. Williams,<sup>5</sup> Daniel A. Hunter,<sup>5</sup> Naresh K. Gunasekar,<sup>5</sup> Paul R. Edwards,<sup>5</sup> Robert W. Martin,<sup>5</sup> Feng Wu,<sup>6</sup> Akhil Mauze,<sup>6</sup> James S. Speck,<sup>6</sup> and Winston V. Schoenfeld<sup>1, 7, 8, a)</sup>

<sup>1)</sup>CREOL, The College of Optics and Photonics, University of Central Florida, 4304 Scorpius St., Orlando, FL 32816, USA

<sup>2)</sup>Department of Electrical and Electronics Engineering, Şırnak University, Şırnak, Türkiye

<sup>3)</sup>Dept. of Physics, Centre for Materials Science and Nanotechnology, Univ. of Oslo, Oslo, Norway

<sup>4)</sup>Lawrence Livermore National Laboratory, Livermore, California 94550, USA

<sup>5)</sup>Department of Physics, SUPA, University of Strathclyde, Glasgow G4 0NG, UK

<sup>6)</sup>Materials Department, University of California Santa Barbara, CA 93106-5050, USA

<sup>7)</sup>Department of Electrical and Computer Engineering, University of Central Florida, Orlando, FL 32816, USA

<sup>8)</sup>Department of Materials Science and Engineering, University of Central Florida, Orlando, FL 32816, USA

(Dated: 10 August 2022)

We report ultra-high responsivity of epitaxial  $(\text{Sn}_x\text{Ga}_{1-x})_2\text{O}_3$  (TGO) Schottky UV-C photodetectors and experimentally identified the source of gain as deep-level defects, supported by first principle calculations. Epitaxial TGO films were grown by plasma-assisted molecular beam epitaxy (PAMBE) on (-201) oriented n-type  $\beta\text{-Ga}_2\text{O}_3$  substrates. Fabricated vertical Schottky devices exhibited peak responsivities as high as  $3.5 \times 10^4$  A/W at -5 V applied bias under 250 nm illumination with sharp cut-off shorter than 280 nm and fast rise/fall time in milliseconds order. Hyperspectral imaging (HSI) cathodoluminescence (CL) spectra were examined to find the mid-bandgap defects, the source of this high gain. Irrespective of different tin mole fractions the TGO epilayer exhibited extra CL peaks at the green band ( $\sim 2.20$  eV) not seen in  $\beta\text{-Ga}_2\text{O}_3$  along with enhancement of the blue emission-band ( $\sim 2.64$  eV) and suppression of the UV emission-band. Based on hybrid functional calculations of the optical emission expected for defects involving Sn in  $\beta\text{-Ga}_2\text{O}_3$ ,  $V_{\text{Ga}}\text{-Sn}$  complexes are proposed as potential defect origins of the observed green and blue emission-bands. Such complexes behave as acceptors that can efficiently trap photogenerated holes and are predicted to be predominantly responsible for the ultra-high photoconductive gain in the Sn-alloyed  $\text{Ga}_2\text{O}_3$  devices by means of thermionic emission and electron tunneling. Regenerating the  $V_{\text{Ga}}\text{-Sn}$  defect complexes by optimizing the growth techniques, we have demonstrated a planar Schottky UV-C photodetector of the highest peak responsivity.

Gallium oxide has become a natural choice for deep UV applications because of its ultra-wide optical bandgap that exceeds  $\sim 4.4$  eV at room temperature (RT).<sup>1</sup> Alloying  $\text{Ga}_2\text{O}_3$  with  $\text{In}^2$ ,  $\text{Al}^3$ , and  $\text{Sn}^4$  can modify the bandgap of the epilayer allowing UV-C optoelectronic devices to be tuned. Among them, tin gallium oxide photodetectors has become a viable path for ultra-high responsivity with shorter transient characteristics than its  $\text{Ga}_2\text{O}_3$  counterparts.<sup>4-6</sup> It has been a challenge to identify the source of high gains in  $\text{Ga}_2\text{O}_3$ -based photodetectors, and recent reports demonstrated its correlation with deep-level defects.<sup>6-9</sup> The fast progress of wide-bandgap metal-oxide relies on the success in understanding and controlling their defects.<sup>10,11</sup> Cathodoluminescence (CL) Hyperspectral imaging (HSI) becoming an invaluable tool for defect metrology because of its ability to map intensity variations or shifts in the emission wavelength.<sup>12</sup> Identifying the nature and the concentration of those defects in a material and further manipulating them to tune the functional properties in a desired manner have become an important part of defect engineering.<sup>13</sup>

In this research, we epitaxially grew TGO layers on (-201) Sn-doped  $\beta\text{-Ga}_2\text{O}_3$  substrates by PAMBE and fabricated vertical Schottky solar-blind UV photodetectors. Considering a planar device and heterojunctions with  $\text{Ga}_2\text{O}_3$ , the reported responsivity ( $3.5 \times 10^4$  A/W) in this paper is the highest for a UV-C Schottky photodetector.<sup>14</sup> We performed X-ray Diffraction and cross-sectional high-resolution transmission electron microscope (HRTEM) to investigate the crystalline quality of the film. An electron probe microanalyzer (EPMA) was used to measure RTCL as well as wavelength dispersive X-ray (WDX) spectroscopy to quantify the Sn composition. CL-HSI spectra were collected and analyzed to investigate optical emission related to deep-level defects.<sup>15</sup> The optical emission energies of Sn-related defects in  $\beta\text{-Ga}_2\text{O}_3$  were estimated utilizing hybrid functional calculations. The epitaxial growth, fabrication and characterization experimental details are described in Supplementary Annexure-A.

To evaluate relative defect solubilities and associated defect level positions, defect formation energies ( $E^f$ ), thermodynamic and vertical transition levels were calculated using the Heyd-Scuseria-Ernzhof screened hybrid functional (HSE06) and projector-augmented wave (PAW) approach as implemented in the VASP code.<sup>16-19</sup> All calculations were performed using supercells with 160-atoms with the same com-

<sup>a)</sup>Authors to whom correspondence should be addressed: partha.mukhopadhyay@creol.ucf.edu, winston@creol.ucf.edu

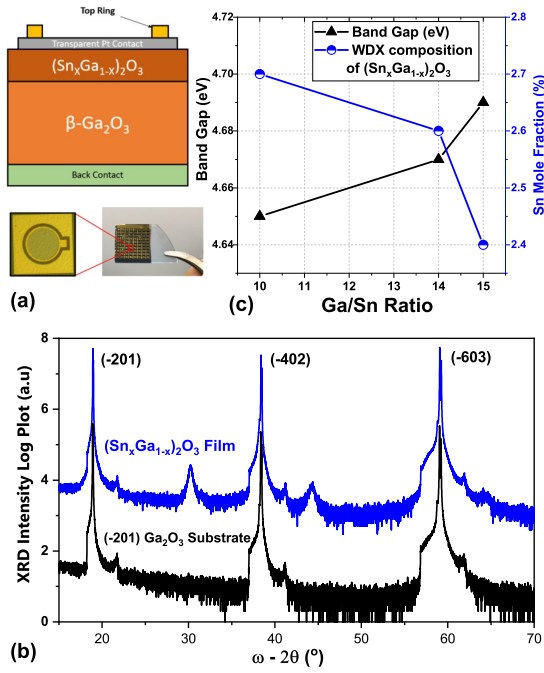


FIG. 1. (a) Schematic of epilayers and fabricated real image of device/sample, b) comparative XRD, c) bandgap and Sn% with MBE flux-ratio.

putational approach and finite size corrections for the formation energies and thermal and vertical transition energies as detailed in other previous publications.<sup>20–22</sup> Configuration coordinate diagrams were constructed with the calculated energies and used to evaluate the resulting optical excitation and emission energies to compare with the experimental spectra. To assess uncertainties in the reduction of the bandgap with Sn-alloying, we provide additional estimates of calculated emission energies assuming the observed redshift in the bandgap occurs in the conduction band only vs including contributions to changes in the valence band position. These choices lead to additional uncertainties in the calculated energies by approximately 0.1 eV.

Fig.1(a) shows cross-section schematic of epilayers and real images of fabricated devices/sample while supplementary Fig.S1 shows the surface morphology. Fig.1(b) XRD plot shows that the TGO epilayers are monoclinic in nature, following the  $Ga_2O_3$  substrate with the major peaks aligned. The two extra peaks at  $\sim 30.28^\circ$  and  $\sim 44.37^\circ$  of the TGO film might be the (-402) and (-604) planes of monoclinic TGO epilayer. However, with the limited XRD database of TGO, it is hard to attribute the right orientation. Thus, we performed cross-sectional HRTEM where we observed that the orientation is slightly modified from monoclinic phase, which needs to be studied further; not the scope of this paper. The tin concentration variation was not much among the samples and consequently, we haven't observed any peak shifting in XRD as we saw in TGO on (010)  $\beta$ - $Ga_2O_3$ <sup>5</sup>, sapphire<sup>4</sup>, and silicon<sup>6</sup> substrates. Tauc Plot in Fig.S2 shows the estimation of the band-gap for various Sn concentrations. This band-gap

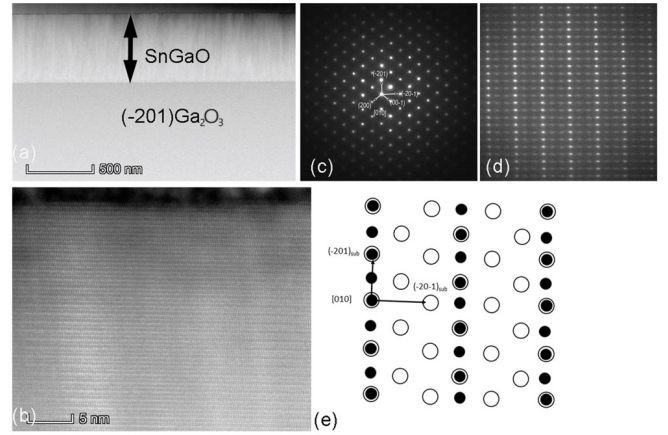


FIG. 2. [010] Cross-sectional TEM images of TGO film and substrate. (a-b) are HAADF images with different magnification. (c) and (d) are SADPs taken from substrate and film, respectively. (e) schematic of SADP, the white spots correspond to the diffraction pattern from substrate, the black spots refer to strong diffraction from the TGO film.

along with Sn% found by WDX plotted in Fig.1(c) with MBE Ga/Sn flux-ratio. A redshift in the bandgap is observed as the Sn incorporation in the TGO is increased. Compositionally uniform epilayer is evident in Fig.S3 WDX cross-sectional images.

The HAADF images in Fig.2(a-b) clearly show the thickness of the epilayer as 500 nm as well as the film quality. Fig.2(c-d) presents the selected area diffraction pattern (SADP) for the substrate and TGO epilayer respectively. When the two SADP images are compared, the growth plane in the film is the same, but additional spots appear in the middle of two adjacent  $(-201)_{sub}$  diffraction spots. Both diffraction patterns are parallel to  $(010)_{sub}$ , which is in the growth plane. The  $(201)_{sub}$  plane is nearly perpendicular to the growth direction which is used to speculate the in-plane orientation relationship between the film and substrate. Fig.2(e) is the schematic of SADP in [010] direction for both film and substrate. The black spots refer to strong diffraction from film, while white spots refer to diffraction from substrate. The diffraction spots, mainly perpendicular to the growth direction for the film, are not only parallel to  $(201)_{sub}$ , but also show a 2:3 spacing ratio. All of the observation and analysis indicate that the microstructure of film has changed due to Sn-alloying. This is likely due to the interplay between the concentrations of incorporated donors like Sn, compensating  $V_{Ga}$  species, and their connection to structural defects or alternative phases inclusions like the  $\gamma$ -phase.<sup>23,24</sup> While in this work we focus on the Sn-related defects in the  $\beta$ -phase as an initial proxy to understanding the origins of the observed emission-bands and measured optical response, further work is needed to better resolve the structure and clarify its role in the device performance and optical behavior.

Fig.3(a) shows the I-V characteristics for a 500  $\mu m$  diameter device of the highest responsivity sample (35 kA/W) in the dark and under UV illumination. Fig.S4 provides the

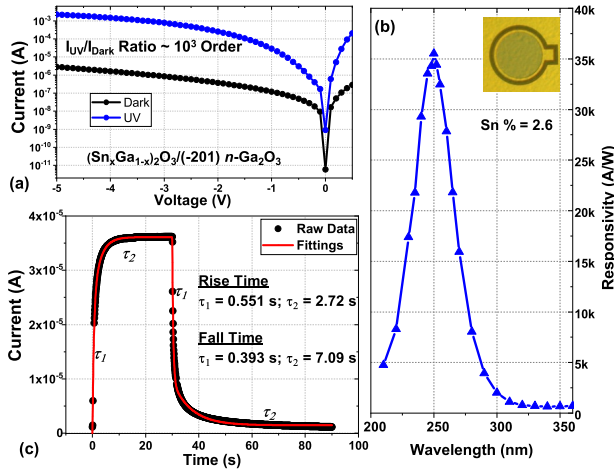


FIG. 3. (a) I-V characteristics, (b) Spectral responsivity of the highest responsivity sample, (c) transient with curve fittings.

measured spectral response of different devices at -5 V. We observe a clear redshift in the 1-dB cutoff below 280 nm as the Sn% increases, consistent with our prior works.<sup>4-6</sup>. The absolute spectral responsivity of the optimized sample in Fig.3(b) validates the solar-blind functionality. Transient measurements, shown in Fig.3(c), were fitted with a double exponential to determine the  $\tau_1$  and  $\tau_2$  times for both the rise and fall segments. The devices'  $\tau_1$  fall times were considerably shorter, with all devices having values in the milliseconds regime. Achieving millisecond order rise/fall times at an extremely high responsivity of 35 kA/W makes TGO devices very fast compared to its counterparts because of the trade-off<sup>14</sup> between response time and gain in the system in the  $Ga_2O_3$ -based Schottky barrier photodetectors.

The optimized sample shows an ultra-high peak responsivity of  $3.5 \times 10^4$  A/W implying that there is a clear gain mechanism since EQE cannot be more than unity. These high-gains are attributed to three main mechanisms in the literature: Impact ionization, Self-Trapped holes (STHs), and hole-trapping in the space-charge region (SCR) in Schottky-barrier diodes. Impact ionization requires a high electric field in the SCR, however, it is not the case with low bias voltages (only -5 V in this work). Likewise, STHs are thermally unstable above 90 K<sup>25</sup>, and a 0.40 eV barrier was calculated for migration of STHs<sup>26</sup>. Therefore, they may not have a noticeable effect at RT. Hole-trapping at the SCR is considered to be the root of the high photoconductive gain by means of deep-level defect states, especially  $V_{Ga}$ .<sup>6,8</sup> Therefore, we propose that Sn-alloying introduces deep-level defects rather than irradiation with fast reactor neutrons, 20 MeV protons, or treatment in high ion density Ar-plasma.<sup>9</sup> This is also consistent with prior reports that confirm the expected correlation between incorporated donor concentrations and native sources of compensation like  $V_{Ga}$  deep acceptors that can readily trap holes.<sup>21,23,24,27,28</sup> To further investigate the deep-level defects, we performed CL spectroscopy and HSI.

Peak positions of all the TGO samples appeared same as shown in Fig.4(a). It also clearly shows the appearance of

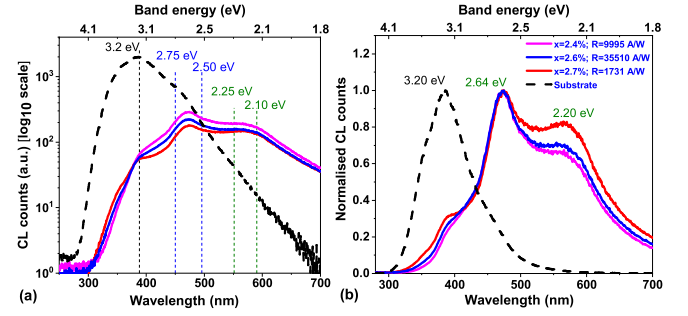


FIG. 4. Comparative CL spectra from TGO samples and  $Ga_2O_3$  substrate excited using a 6 keV electron beam; (a) absolute CL intensity in  $\log_{10}$  scale, (b) normalized intensity.

peaks (mid-gap donor/acceptor level) at blue ( $\sim 2.50$ - $2.75$  eV) and green bands ( $\sim 2.10$ - $2.25$  eV), which are not present in the substrate. Deconvolving the spectra identifies the peak positions as  $\sim 2.64$  eV and  $\sim 2.20$  eV which can clearly be seen in Fig.4(b) where the normalized CL intensities are plotted for both the TGO films and the substrate.

Moreover, in the TGO films, the UV-range peak intensity is lower and that of the blue emission is greater compared to the  $Ga_2O_3$  substrate. We have not observed any definite correlation between CL peak intensity variations with Sn% among the samples. Intrinsic point-defects in  $Ga_2O_3$  such as  $V_{Ga}$  and oxygen vacancies ( $V_O$ ) exhibit distinct dependencies on the ambient, doping, defect concentrations, and their relative populations can influence the absorption and luminescence characteristics.<sup>29-33</sup> In Fig.4(b), the UV band is found to be diminished in the TGO film relative to the bulk  $Ga_2O_3$ , which indicates the enhancement of other recombination channels not associated with intrinsic hole-trapping in the form of STHs.<sup>32</sup> Regarding the second intrinsic point defect, we first note that the TGO films are found to be modestly n-type by CV measurement ( $n \sim 10^{17} \text{ cm}^{-3}$ ), despite their large Sn concentration. This suggests significant compensation of incorporated Sn donors, consistent with the formation of a larger number of compensating acceptor species such as  $V_{Ga}$  that become more favorable in n-type conditions.<sup>21,23,24,27,28,34</sup>  $V_{Ga}$  is also known to form a number of complexes with other intrinsic and extrinsic donor defects such as  $V_O$ ,  $H^{35,36}$ , and  $Sn^{23,28}$  because of the Coulomb attraction between positively charged donors and the triply negatively charged  $V_{Ga}$ . This results in highly stable complexes with large binding energies such as 1.63 eV for the most stable forms of  $V_{Ga}$ -Sn complexes in n-type material. We have mentioned earlier that the 2.20 eV and 2.64 eV peaks are not present in neither the  $Ga_2O_3$  substrate nor MBE grown  $Ga_2O_3$  homoepitaxial layer. The incorporation of Sn donors into the  $Ga_2O_3$  crystal lattice may well have increased the concentration of compensatory  $V_{Ga}$  and  $V_{Ga}$ -Sn complexes, which will be investigated in the subsequent paragraphs.

To further interrogate the role of Sn, WDX and CL HSI was performed as shown in Fig.5. The observed emission spectra are uniform over the cross-section of the TGO epilayers. Fig.5(a) shows a map of the Sn WDX counts identi-

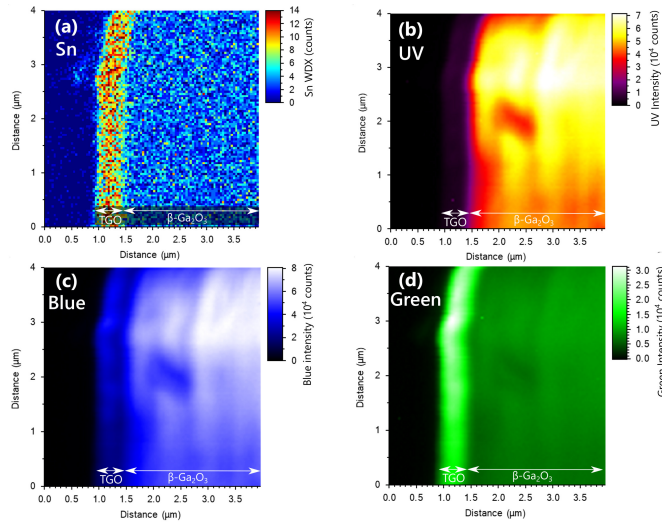


FIG. 5. Cross-sectional WDX and CL-HSI of the TGO film and substrate. Images showing the intensity of (a) Sn WDX X-ray counts, and emission peaks of (b) UV, (c) blue, (d) green.

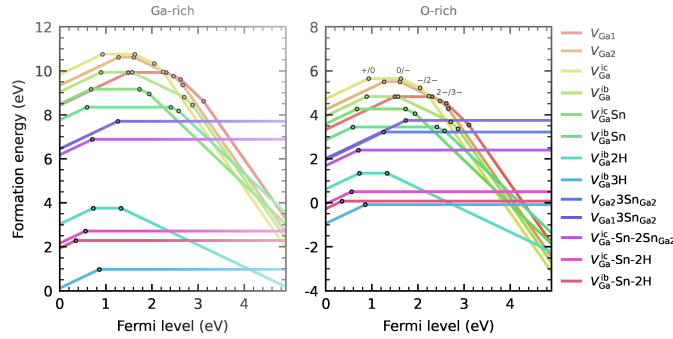


FIG. 6. Formation energy diagram for  $V_{Ga}$  and related complexes with H and Sn shown for (a) Ga-rich and (b) O-rich conditions

fyng the TGO layer and the  $Ga_2O_3$  substrate. The UV-blue emission peak intensity is reduced in the presence of Sn as shown in Fig.5(b) and (c), respectively. In addition, Fig.5(d) demonstrates that the green emission peak is consolidated in the TGO film, with an intensity far greater than in the Sn-doped substrate, which is further evidence of this emission peak being related to Sn and/or  $V_{Ga}$  complexes, as previously stated.

Fig.6 plots the calculated formation energies for  $V_{Ga}$  and a number of complexes that may form with H and/or Sn. We primarily consider the displaced, or “split” vacancy configurations (e.g.  $V_{Ga}^{ic}$  and  $V_{Ga}^{ib}$ ) that have been previously shown to be favorable configurations for isolated  $V_{Ga}$  and their complexes with H and Sn.<sup>23,27,35</sup> These complexes can form with Sn or Ga as the displaced atom that occupies the interstitial position (ic or ib), with  $Sn^{ic}$  or  $Sn^{ib}$  being the more thermodynamically-preferable configurations, and labeled in Fig.6 as  $V_{Ga}^{ic}Sn$  or  $V_{Ga}^{ib}Sn$ , respectively. We also include formation energies for  $V_{Ga}$  on the tetrahedral ( $Ga_I$ ) and octahedral ( $Ga_{II}$ ) sites, with different neighboring  $Sn_{Ga_{II}}$  configura-

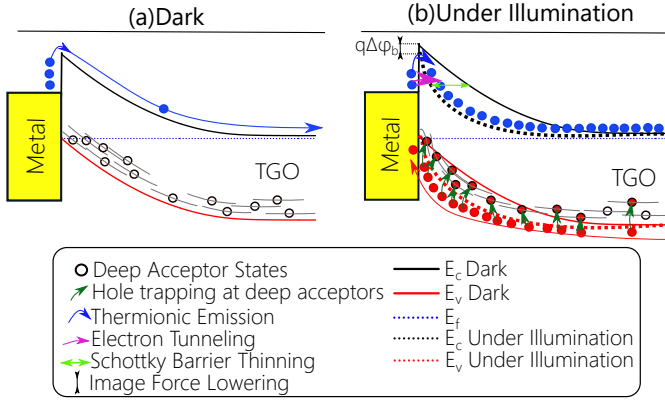
tions. These results illustrate the strong driving force to form compensating  $V_{Ga}$  acceptor complexes as the Fermi level is pushed to more n-type conditions, and how fully-passivated complexes can also be favorable (e.g.  $V_{Ga}$ -3H,  $V_{Ga}$ -3 $Sn_{Ga}$ , and  $V_{Ga}$ - $Sn_{Ga}$ -2H, among others). Table I presents the calculated emission for the defects, from which we find the best matches for the 2.64 eV band in the TGO films that result from electron recombination with trapped hole states associated with a number of different vacancy configurations. In particular, we find that recombination of a free electron with a hole trapped on isolated ( $V_{Ga}^{ic}$ )<sup>+</sup> and ( $V_{Ga}^{ib}$ )<sup>+</sup> configurations or their complexes with Sn (e.g. ( $V_{Ga}^{ic}$ -Sn)<sup>+</sup>) exhibit an emission between  $\sim 2.6$ -2.7 eV. This is consistent with previous theoretical calculations reporting emission  $\sim 2.6$  eV for  $V_{Ga}$ -Sn complexes.<sup>28</sup> However, we find the donor charge-states of these defects to be unlikely in n-type conditions, as they would need to be ionized from the -3 charge-state, and thus consider other more passivated forms such as the  $V_{Ga}$  decorated with one or more Sn. Indeed, we find that analogs such as a  $V_{Ga}$ - $Sn^{ic}$  complex with 1 or 2 neighboring  $Sn_{Ga}$ , form more passivated centers in n-type conditions that exhibit  $\sim 2.6$  eV emission-bands for free electrons recombining with holes trapped at these centers. This suggests that under optical excitation, hole-trapping at a number of different defects such as these  $V_{Ga}$  complexes that are enhanced in the TGO can lead to the 2.6 eV emission-band.

For the 2.20 eV band, we find a qualitatively analogous origin as the 2.64 eV band, but originating from defects involving  $V_{Ga_{II}}$  orientations rather than the split-vacancy configurations. For example, we find the best agreement from the studied defects to be from the recombination of free electrons with holes trapped at the  $V_{Ga_{II}}^+$  donor-state or the fully-passivated  $V_{Ga_{II}}$ -3 $Sn_{Ga}$  complex yielding emission energies of 2.16 eV and 2.23 eV, respectively. We note that the binding-energies of  $V_{Ga_{II}}$  with multiple Sn is reasonably large, with the 3rd Sn-binding more stable by 0.94 eV relative to isolated ( $V_{Ga_{II}}$ -2 $Sn_{Ga}$ )<sup>-</sup> and  $Sn_{Ga}^+$ , suggesting these complexes are likely to be stable if formed. Considering this modest complex binding strength, the high surface mobility of Sn<sup>37</sup>, and the large degree of compensation of the incorporated Sn in the TGO films, these complexes are likely candidates for the 2.20 eV band. This may also be supported by the lower relative intensities of the 2.20 eV band, as the split-vacancy configurations are predicted to be more thermodynamically favorable and likely to form in higher concentrations in the absence of other kinetic hindrances that may result from complexing. Lastly, we note that the presence of interstitial H and its passivation of  $V_{Ga}$  and  $V_{Ga}$ -Sn complexes may also influence the relative stability of these defects and their charge-states, and may contribute to shifts in some of the emission-bands as seen in Table I. While Sn-related defects are expected to dominate in these samples based on their concentrations, the effects of H on these bands will be investigated in more detail in future publications.

Among the three gain mechanisms mentioned, impact ionization and STHs are not likely contributors. Hole-trapping at the deep-level defects in the SCR is considered to be the root of the high photoconductive gain by lowering the Schottky barrier height in  $Ga_2O_3$ .<sup>8</sup> Recently, we reported TGO on Si

TABLE I. CC model parameters for  $V_{Ga}$  complexed with Sn and H donors, including ZPL energy ( $E_{ZPL}$ ), classical emission ( $E_{em}$ ) and absorption ( $E_{abs}$ ) energies, total mass-weighted distortion ( $\Delta Q$ ). Obtained from HSE(0.33,0.20) dv calculations.

Optical transition	$E_{ZPL}$ (eV)	$E_{em}$ (eV)	$E_{abs}$ (eV)	$\Delta Q(amu^{1/2}/\text{\AA})$
$(V_{Ga}^{ib})^+ + e_{CMB}^-$	4.25	2.69	5.1	2.67
$(V_{Ga}^{ic})^+ + e_{CMB}^-$	3.97	2.56	5	2.81
$V_{Ga2}^+ + e_{CMB}^-$	3.62	2.16	4.92	2.79
$V_{Ga1}^+ + e_{CMB}^-$	3.4	1.94	4.75	2.47
$(V_{Ga}^{ic}Sn)^- + e_{CBM}^-$	2.95	1.51	4.27	2.42
$(V_{Ga}^{ic}Sn)^0 + e_{CBM}^-$	3.17	1.62	4.48	2.46
$(V_{Ga}^{ic}Sn)^+ + e_{CBM}^-$	4.16	2.7	5.16	2.78
$(V_{Ga}^{ib}Sn)^- + e_{CBM}^-$	2.32	0.91	3.67	2.34
$(V_{Ga}^{ib}Sn)^0 + e_{CBM}^-$	2.49	1.1	3.83	2.35
$(V_{Ga}^{ib}Sn)^+ + e_{CBM}^-$	4.31	2.73	5.05	2.74
$(V_{Ga}^{ic}Sn-SnGa2)^0 + e_{CBM}^-$	3.22	1.83	4.45	2.41
$(V_{Ga}^{ic}Sn-SnGa2)^+ + e_{CBM}^-$	4.07	2.64	5.09	2.82
$(V_{Ga}^{ic}Sn-2SnGa2)^+ + e_{CBM}^-$	4	2.61	5.11	2.86
$(V_{Ga2}2SnGa2)^0 + e_{CBM}^-$	3.14	1.8	4.33	2.03
$(V_{Ga2}3SnGa2)^+ + e_{CBM}^-$	3.64	2.23	4.83	2.15
$(V_{Ga1}3SnGa2)^+ + e_{CBM}^-$	3.15	1.79	4.36	2.19
$(V_{Ga}^{ib}2H)^0 + e_{CBM}^-$	3.57	2	4.81	2.59
$(V_{Ga}^{ib}3H)^+ + e_{CBM}^-$	3.95	2.5	5.1	2.7
$(V_{Ga}^{ib}Sn-H)^0 + e_{CBM}^-$	2.52	1.12	2.83	2.28
$(V_{Ga}^{ic}Sn-H)^0 + e_{CBM}^-$	3.2	1.77	4.49	2.47
$(V_{Ga}^{ib}Sn-2H)^+ + e_{CBM}^-$	4.54	2.97	5.07	2.82
$(V_{Ga}^{ic}Sn-2H)^+ + e_{CBM}^-$	4.33	2.86	5.04	2.7

FIG. 7. The proposed gain mechanism via deep-level acceptor states introduced by Sn incorporation into the  $Ga_2O_3$  crystal lattice. (a) Carrier transport in TGO under dark conditions. (b) Hole-trapping-assisted gain mechanism under UV illumination in TGO photodetectors.

films showing enhanced blue and green emission, which was attributed to the deep-level acceptors.<sup>6</sup> This correlation and the gain is higher in the present work along with faster PDs,

thanks to single crystal TGO epilayer. Moreover, based on hybrid functional calculations of the optical emission expected for defects involving Sn in  $\beta-Ga_2O_3$ ,  $V_{Ga}$ -Sn complexes with the possibility of additional  $H_i$  are proposed as potential defect origins of the observed green and blue emission-bands. These complexes increase the deep-level trap states and can serve as hole-trapping centers as illustrated in Fig.7. The accumulated holes in the SCR via trapping to the deep acceptor sites increase the total positive charge. Thereby, the electric field in the SCR increases. Higher surface electric field ( $E_{max}$ ) lowers the Schottky barrier via image-force lowering ( $\Delta\Phi_b = \sqrt{(qE_{max}/4\pi\epsilon_s)}$ , and thins the barrier width.<sup>38</sup> Thereby, it exponentially enhances thermionic emission and the probability of electron tunneling, which leads to high gains as demonstrated in this work. Li et al. have demonstrated that near-ideal barrier tunneling governs dark current characteristics for  $E_{max}$  greater than 0.8 MV/cm.<sup>39</sup> They also investigated the electric-field threshold (ET) above which the dominant current mechanism switches from thermionic emission to electron tunneling.<sup>40</sup> They found that, at RT, ET is about 0.3MV/cm, which means that even at moderate electric fields, electron tunneling is an effective mechanism. Given adequate hole-trapping at the aforementioned deep-level acceptors, both the Schottky effect and electron tunneling may

be the major sources in the gain mechanism of TGO Schottky-barrier photodetectors. Furthermore, alloying broadens the UV-C coverage and increases the bandwidth of the resultant photodetector.

In conclusion, the TGO planar solar-blind Schottky photodetector demonstrated a record-setting responsivity of 35510 A/W at -5 V. Defect-induced mid-bandgap donor/acceptor levels were found to be playing a key role in trapping holes and thereby, enhancing the photoconductive gain. RTCL spectra and HSI depict clear peak appearances at 2.64 eV and 2.20 eV, which are not present in the  $Ga_2O_3$  substrate as well as MBE-grown  $Ga_2O_3$  homoepitaxial layer. UV-emission-bands in the substrate and  $Ga_2O_3$  epilayers are suppressed in the TGO films, suggesting either a redistribution of defect populations and/or preferential recombination channels. The first principle calculations identify the nature of defect levels to be  $V_{Ga}$  complexes with one or more Sn and possibly H that lead to passivated complexes that can trap holes and lead to the dominant emission-bands in the TGO films. Hole-trapping at these deep-level defects in the SCR is found to be responsible for the exponential increase of photocurrent by lowering the Schottky barrier height via the Schottky effect, and electron tunneling via lowering the barrier height and thinning the barrier width. This study investigates how Sn influences the mid-bandgap defect levels and enhances the figure-of-merit of the photodetector which is much superior to its planar device counterparts and possesses record-high responsivity for UV-C solar-blind photodetector.

See the supplementary material for the details of the growth, fabrication, and characterization experiments. Furthermore, we presented results and analysis from various experiments like secondary electron imaging (Fig.S1), room temperature optical bandgap estimations (Fig.S2), WDX mapping (Fig.S3), spectral responsivity measurements (Fig.S4). In addition, further device parameters (Table S1) and intensity-dependent responsivity (Fig.S5) and response time (Fig.S6) are included to depict opto-electronic properties of the photodetectors.

W.V.S., P.M., I.H. would like to acknowledge support from the Army Research Office, monitored by Dr. Michael Gerhold. I.H. was supported by Ministry of National Education of the Republic of Türkiye. This work was partly supported by the EPSRC project “Nanoanalysis for Advanced Materials and Healthcare” (No. EP/N010914/1). The work by J.B.V. was partially performed under the auspices of the U.S. DOE by Lawrence Livermore National Laboratory under contract DE-AC52-07NA27344, and partially supported by the Critical Materials Institute and LLNL LDRD funding under project number 22-SI-003. Y. K. F. was supported by the Research Council of Norway through the GO-POW project (Grant No. 314017).

<sup>1</sup>T. Onuma, S. Saito, K. Sasaki, T. Masui, T. Yamaguchi, T. Honda, and M. Higashiwaki, “Valence band ordering in  $\beta$ - $ga_2o_3$  studied by polarized transmittance and reflectance spectroscopy,” *Japanese Journal of Applied Physics* **54**, 112601 (2015).

<sup>2</sup>I. Hatipoglu, P. Mukhopadhyay, F. Alema, T. S. Sakhivel, S. Seal, A. Osinsky, and W. V. Schoenfeld, “Tuning the responsivity of monoclinic solar-blind photodetectors grown by metal organic chemical vapor deposition,” *Journal of Physics D: Applied Physics* **53**, 454001 (2020).

<sup>3</sup>T. Oshima, T. Okuno, N. Arai, Y. Kobayashi, and S. Fujita, “ $\beta$ - $al_2xga_2-2xo_3$  thin film growth by molecular beam epitaxy,” *Japanese Journal of Applied Physics* **48**, 070202 (2009).

<sup>4</sup>P. Mukhopadhyay and W. V. Schoenfeld, “Tin gallium oxide solar-blind photodetectors on sapphire grown by molecular beam epitaxy,” *Applied Optics* **58**, D22–D27 (2019).

<sup>5</sup>P. Mukhopadhyay and W. V. Schoenfeld, “High responsivity tin gallium oxide schottky ultraviolet photodetectors,” *Journal of Vacuum Science&Technology A: Vacuum, Surfaces, and Films* **38**, 013403 (2020).

<sup>6</sup>I. Hatipoglu, D. A. Hunter, P. Mukhopadhyay, M. S. Williams, P. R. Edwards, R. W. Martin, W. V. Schoenfeld, and G. Naresh-Kumar, “Correlation between deep-level defects and functional properties of  $\beta$ -(sn x ga1-x)  $2o_3$  on si photodetectors,” *Journal of Applied Physics* **130**, 204501 (2021).

<sup>7</sup>P. Mukhopadhyay, I. Hatipoglu, T. S. Sakhivel, D. A. Hunter, P. R. Edwards, R. W. Martin, G. Naresh-Kumar, S. Seal, and W. V. Schoenfeld, “High figure-of-merit gallium oxide uv photodetector on silicon by molecular beam epitaxy: a path toward monolithic integration,” *Advanced Photonics Research* **2**, 2000067 (2021).

<sup>8</sup>E. Yakimov, A. Polyakov, I. Shchemerov, N. Smirnov, A. Vasilev, P. Vergeles, E. Yakimov, A. Chernykh, A. Shikoh, F. Ren, *et al.*, “Photosensitivity of  $ga_2o_3$  schottky diodes: effects of deep acceptor traps present before and after neutron irradiation,” *APL Materials* **8**, 111105 (2020).

<sup>9</sup>E. Yakimov, A. Polyakov, I. Shchemerov, N. Smirnov, A. Vasilev, A. Kochkova, P. Vergeles, E. Yakimov, A. Chernykh, M. Xian, *et al.*, “On the nature of photosensitivity gain in  $ga_2o_3$  schottky diode detectors: Effects of hole trapping by deep acceptors,” *Journal of Alloys and Compounds* **879**, 160394 (2021).

<sup>10</sup>F. Gunkel, D. V. Christensen, Y. Chen, and N. Pryds, “Oxygen vacancies: The (in) visible friend of oxide electronics,” *Applied physics letters* **116**, 120505 (2020).

<sup>11</sup>H. J. Queisser and E. E. Haller, “Defects in semiconductors: some fatal, some vital,” *Science* **281**, 945–950 (1998).

<sup>12</sup>P. R. Edwards and R. W. Martin, “Cathodoluminescence nanocharacterization of semiconductors,” *Semiconductor Science and Technology* **26**, 064005 (2011).

<sup>13</sup>H. Y. Hwang, Y. Iwasa, M. Kawasaki, B. Keimer, N. Nagaosa, and Y. Tokura, “Emergent phenomena at oxide interfaces,” *Nature materials* **11**, 103–113 (2012).

<sup>14</sup>D. Kaur and M. Kumar, “A strategic review on gallium oxide based deep-ultraviolet photodetectors: recent progress and future prospects,” *Advanced optical materials* **9**, 2002160 (2021).

<sup>15</sup>P. R. Edwards, L. K. Jagadamma, J. Bruckbauer, C. Liu, P. Shields, D. Allsopp, T. Wang, and R. W. Martin, “High-resolution cathodoluminescence hyperspectral imaging of nitride nanostructures,” *Microscopy and Microanalysis* **18**, 1212–1219 (2012).

<sup>16</sup>J. Heyd, G. E. Scuseria, and M. Ernzerhof, “Hybrid functionals based on a screened coulomb potential,” *The Journal of chemical physics* **118**, 8207–8215 (2003).

<sup>17</sup>P. E. Blöchl, “Projector augmented-wave method,” *Physical review B* **50**, 17953 (1994).

<sup>18</sup>G. Kresse and J. Furthmüller, “Efficiency of ab-initio total energy calculations for metals and semiconductors using a plane-wave basis set,” *Computational materials science* **6**, 15–50 (1996).

<sup>19</sup>G. Kresse and J. Furthmüller, “Efficient iterative schemes for ab initio total-energy calculations using a plane-wave basis set,” *Physical review B* **54**, 11169 (1996).

<sup>20</sup>C. Freysoldt, B. Grabowski, T. Hickel, J. Neugebauer, G. Kresse, A. Janotti, and C. G. Van de Walle, “First-principles calculations for point defects in solids,” *Reviews of modern physics* **86**, 253 (2014).

<sup>21</sup>Y. K. Frodason, K. Johansen, L. Vines, and J. Varley, “Self-trapped hole and impurity-related broad luminescence in  $\beta$ - $ga_2o_3$ ,” *Journal of Applied Physics* **127**, 075701 (2020).

<sup>22</sup>T. Gake, Y. Kumagai, C. Freysoldt, and F. Oba, “Finite-size corrections for defect-involving vertical transitions in supercell calculations,” *Physical Review B* **101**, 020102 (2020).

<sup>23</sup>J. M. Johnson, Z. Chen, J. B. Varley, C. M. Jackson, E. Farzana, Z. Zhang, A. R. Arehart, H.-L. Huang, A. Genc, S. A. Ringel, *et al.*, “Unusual formation of point-defect complexes in the ultrawide-band-gap semiconductor  $\beta$ - $ga_2 o_3$ ,” *Physical Review X* **9**, 041027 (2019).

<sup>24</sup>C. S. Chang, N. Tanen, V. Protasenko, T. J. Asel, S. Mou, H. G. Xing,

- D. Jena, and D. A. Muller, “ $\gamma$ -phase inclusions as common structural defects in alloyed  $\beta$ -(al x ga $1-x$ )<sub>2</sub>O<sub>3</sub> and doped  $\beta$ -Ga<sub>2</sub>O<sub>3</sub> films,” *APL Materials* **9**, 051119 (2021).
- <sup>25</sup>B. E. Kananen, N. C. Giles, L. E. Halliburton, G. Foundos, K. Chang, and K. Stevens, “Self-trapped holes in  $\beta$ -Ga<sub>2</sub>O<sub>3</sub> crystals,” *Journal of Applied Physics* **122**, 215703 (2017).
- <sup>26</sup>J. B. Varley, A. Janotti, C. Franchini, and C. G. Van de Walle, “Role of self-trapping in luminescence and p-type conductivity of wide-band-gap oxides,” *Physical Review B* **85**, 081109 (2012).
- <sup>27</sup>M. E. Ingebrigtsen, A. Y. Kuznetsov, B. G. Svensson, G. Alfieri, A. Mihailescu, U. Badstübner, A. Perron, L. Vines, and J. B. Varley, “Impact of proton irradiation on conductivity and deep level defects in  $\beta$ -Ga<sub>2</sub>O<sub>3</sub>,” *APL Materials* **7**, 022510 (2019).
- <sup>28</sup>A. Singh, O. Koksal, N. Tanen, J. McCandless, D. Jena, H. G. Xing, H. Peelaers, and F. Rana, “Ultrafast dynamics of gallium vacancy charge states in  $\beta$ -Ga<sub>2</sub>O<sub>3</sub>,” *Physical Review Research* **3**, 023154 (2021).
- <sup>29</sup>M. D. McCluskey, “Point defects in Ga<sub>2</sub>O<sub>3</sub>,” *Journal of Applied Physics* **127**, 101101 (2020).
- <sup>30</sup>H. Peelaers, J. L. Lyons, J. B. Varley, and C. G. Van de Walle, “Deep acceptors and their diffusion in Ga<sub>2</sub>O<sub>3</sub>,” *APL Materials* **7**, 022519 (2019).
- <sup>31</sup>Z. Wang, X. Chen, F.-F. Ren, S. Gu, and J. Ye, “Deep-level defects in gallium oxide,” *Journal of Physics D: Applied Physics* **54**, 043002 (2020).
- <sup>32</sup>Q. D. Ho, T. Frauenheim, and P. Deák, “Origin of photoluminescence in  $\beta$ -Ga<sub>2</sub>O<sub>3</sub>,” *Physical Review B* **97**, 115163 (2018).
- <sup>33</sup>C. Zimmermann, V. Rønning, Y. K. Frodason, V. Bobal, L. Vines, and J. Varley, “Primary intrinsic defects and their charge transition levels in  $\beta$ -Ga<sub>2</sub>O<sub>3</sub>,” *Physical Review Materials* **4**, 074605 (2020).
- <sup>34</sup>T. Zacherle, P. Schmidt, and M. Martin, “Ab initio calculations on the defect structure of  $\beta$ -Ga<sub>2</sub>O<sub>3</sub>,” *Physical Review B* **87**, 235206 (2013).
- <sup>35</sup>J. B. Varley, H. Peelaers, A. Janotti, and C. G. Van de Walle, “Hydrogenated cation vacancies in semiconducting oxides,” *Journal of Physics: Condensed Matter* **23**, 334212 (2011).
- <sup>36</sup>Y. K. Frodason, C. Zimmermann, E. F. Verhoeven, P. M. Weiser, L. Vines, and J. B. Varley, “Multistability of isolated and hydrogenated Ga-O divacancies in  $\beta$ -Ga<sub>2</sub>O<sub>3</sub>,” *Physical Review Materials* **5**, 025402 (2021).
- <sup>37</sup>M. Kracht, A. Karg, J. Schörmann, M. Weinhold, D. Zink, F. Michel, M. Rohnke, M. Schowalter, B. Gerken, A. Rosenauer, *et al.*, “Tin-assisted synthesis of  $\epsilon$ -Ga<sub>2</sub>O<sub>3</sub> by molecular beam epitaxy,” *Physical Review Applied* **8**, 054002 (2017).
- <sup>38</sup>S. M. Sze, Y. Li, and K. K. Ng, *Physics of semiconductor devices* (John Wiley & sons, 2021).
- <sup>39</sup>W. Li, D. Saraswat, Y. Long, K. Nomoto, D. Jena, and H. G. Xing, “Near-ideal reverse leakage current and practical maximum electric field in  $\beta$ -Ga<sub>2</sub>O<sub>3</sub> Schottky barrier diodes,” *Applied Physics Letters* **116**, 192101 (2020).
- <sup>40</sup>W. Li, K. Nomoto, D. Jena, and H. G. Xing, “Thermionic emission or tunneling? the universal transition electric field for ideal Schottky reverse leakage current: a case study in  $\beta$ -Ga<sub>2</sub>O<sub>3</sub>,” *Applied Physics Letters* **117**, 222104 (2020).